SIAM J. Appl. Math.
Vol. 0, No. 0, pp. 000–000

APPLICATION OF THE INHOMOGENEOUS LIPPMANN–SCHWINGER EQUATION TO INVERSE SCATTERING PROBLEMS*

GIOVANNI GIORGI†, MASSIMO BRIGNONE‡, RICCARDO ARAMINI†, AND MICHELE PIANA§

Abstract. In this paper we present a hybrid approach to numerically solving two-dimensional electromagnetic inverse scattering problems, whereby the unknown scatterer is hosted by a possibly inhomogeneous background. The approach is "hybrid" in that it merges a qualitative and a quantitative method to optimize the way of exploiting the a priori information on the background within the inversion procedure, thus improving the quality of the reconstruction and reducing the data amount necessary for a satisfactory result. In the qualitative step, this a priori knowledge is utilized to implement the linear sampling method in its near-field formulation for an inhomogeneous background, in order to identify the region where the scatterer is located. On the other hand, the same a priori information is also encoded in the quantitative step by extending and applying the contrast source inversion method to what we call the "inhomogeneous Lippmann–Schwinger equation"; the latter is a generalization of the classical Lippmann–Schwinger equation to the case of an inhomogeneous background, and in our paper is deduced from the differential formulation of the direct scattering problem to provide the reconstruction algorithm with an appropriate theoretical basis. Then the point values of the refractive index are computed only in the region identified by the linear sampling method at the previous step. The effectiveness of this hybrid approach is supported by numerical simulations presented at the end of the paper.

Key words. inverse scattering, Lippmann–Schwinger equation, hybrid methods

AMS subject classifications. 78A46, 45Q05

DOI. 10.1137/120869584

1. Introduction.

Acoustic, elastic, or electromagnetic scattering is a physical phenomenon where an incident wave is scattered by an inhomogeneity (or an obstacle) and the total field at any point is represented by the sum of the incident and the scattered field. From a mathematical viewpoint, in the direct problem the physical parameters and the geometry of the inhomogeneity are given and the unknown is represented by the scattered field. In the inverse scattering problem, one aims at recovering the shape and the physical properties of the object of interest from measurements of the scattered field. The direct scattering problem is in general well-posed in the sense of Hadamard, and therefore its approximate solution can be determined by means of stable numerical methods. On the contrary, the inverse scattering problem is ill-posed in the sense of Hadamard (specifically, the unknown physical parameters of the scatterer are mapped onto the measured scattered field by a compact operator), and its solution must be addressed by means of some regularizing approach [11].

Most inverse scattering methods belong to two different sets of algorithms: the family of qualitative approaches and the family of quantitative approaches. Qualita-

*Received by the editors March 12, 2012; accepted for publication (in revised form) September 27, 2012; published electronically DATE.
http://www.siam.org/journals/siap/x-x/86958.html
†Dipartimento di Matematica, Università di Genova, via Dodecaneso 35, I-16146 Genova, Italy (giorgi@dima.unige.it, aramini@dima.unige.it).
‡Azienda Ospedaliera Universitaria San Martino, Largo Benzi 10, I-16132 Genova, Italy (brignone@dima.unige.it).
§Dipartimento di Matematica, Università di Genova, via Dodecaneso 35, I-16146 Genova, Italy and CNR - SPIN, Genova, via Dodecaneso 33, I-16146 Genova, Italy (piana@dima.unige.it).

tive methods [8] require the regularized solution of a linear integral equation of the first kind, parameterized over a grid of sampling points covering the investigation domain. The Euclidean norm of such regularized solution behaves as an indicator function of the unknown scatterer, since it is bounded when the sampling point is inside the target, grows up if the point approaches its edge, and can be made arbitrarily large when it is taken outside. The advantages of qualitative methods are that they are fast and need very few a priori information to work. However, the informative content of their output is rather poor, since they are essentially visualization techniques and do not provide quantitative reconstructions of the inhomogeneity.

On the other hand, quantitative inverse scattering methods [3, 11] are, in general, iterative schemes that minimize an appropriate functional, starting from an initialization mask for the refractive index of the scatterer, and then reconstruct its point values after an optimized number of iterations. In principle, they can provide all the required information on the problem, although by means of a notable computational effort. However, they can suffer from local minima problems, since the number of unknowns is typically larger than the data amount at disposal in scattering experiments, or because often the initialization of the method is not precise enough for a proper convergence to the solution. The effectiveness of a quantitative method can be notably increased by incorporating some a priori information (when available) on the scatterer into the minimization process. Although the most traditional approach is to use this knowledge for a better initialization of the algorithm, an improvement in its performance can be achieved when such information is integrated into each step of the iterative scheme, e.g., by decreasing the complexity of the target [14], or by adding appropriate constraints to the minimization technique [28].

Recent developments in inverse scattering are concerned with the formulation of hybrid methods, i.e., methods merging different techniques in order to integrate and optimize the different kinds of information they can provide (see, e.g., [6, 7, 18]). In particular, a priori knowledge on the scatterer and/or qualitative techniques are typically utilized to improve the performance of some quantitative method, e.g., by reducing the number of unknowns, or by providing a more precise initialization. In this paper, we rely on a rather general strategy for the formulation of hybrid techniques, based on the following three steps:

1. the a priori information on the physical characteristics of the (possibly inhomogeneous) background is coded into the corresponding Green's function;
2. a segmentation between the background and the scatterer is realized by applying a qualitative method, thus reducing the size of the investigation domain, i.e., the number of unknowns in the following step;
3. a quantitative method is applied only in the region highlighted by the qualitative method, in order to reconstruct the point values of the refractive index in this region.

Although this scheme is of general applicability, in this paper we present a specific implementation: more precisely, the Green's function of the (inhomogeneous) background is numerically computed by means of the method of moments [15, 25], which solves the forward scattering problem. Then the linear sampling method [13] is applied in its near-field formulation for inhomogeneous backgrounds [9, 12] in order to visualize the scatterer of interest, and a procedure based on active contours [1, 10] is used for extracting the (approximate) shape of its support. Finally, the inverse scattering problem is solved by generalizing and applying the contrast source inversion method [14, 27, 28] to what we call the "inhomogeneous Lippmann–Schwinger equation," since it is a generalization of the integral formulation of the direct scattering

problem to the case of an inhomogeneous background: such an equation is deduced in our paper as a preliminary but essential tool that allows encoding the a priori information on the background into each step of the iterative reconstruction procedure. Note that the initial qualitative approach allows computing the point values of the refractive index only in the region identified by the linear sampling method, thus reducing the number of unknowns to be determined by the quantitative method.

The plan of the paper is as follows. In section 2 we introduce the differential formulation of the direct scattering problem and recall some known results. Section 3 addresses the same problem from an integral perspective, and as a result the inhomogeneous Lippmann–Schwinger equation is derived from the direct differential formulation. In section 4 we recall the key ideas of the linear sampling method in the near-field case and adapt the contrast source inversion method to the inhomogeneous Lippmann–Schwinger equation. In section 5 some numerical examples are described, also including an application to breast cancer detection by using microwaves. Finally, our conclusions are offered in section 6.

2. The scattering problem: Differential formulation. We consider a rather general two-dimensional and time-harmonic scattering problem, whereby the background medium is inhomogeneous and described by a piecewise continuously differentiable refractive index [11, 12]

$$n_b(x) = \frac{1}{\varepsilon_0}\left[\varepsilon(x) + \mathrm{i}\frac{\sigma(x)}{\omega}\right]. \tag{2.1}$$

In (2.1), $x = (x_1, x_2)$ is a generic point of $\mathbb{R}^2$, $\varepsilon_0 > 0$ is the dielectric permittivity of vacuum, $\varepsilon(x) \geq 1$ and $\sigma(x) \geq 0$ are the point values of the dielectric permittivity and conductivity of the medium, ω is the angular frequency, and $\mathrm{i} = \sqrt{-1}$. More precisely (see, e.g., Figure 1), we assume that there exists a finite number $N+1$ of open and connected C^2-domains $\Omega_i \subset \mathbb{R}^2$, with $i = 0, \ldots, N$, such that (1) $\Omega_i \cap \Omega_j = \emptyset$ for $i \neq j$; (2) $\mathbb{R}^2 = \cup_{i=0}^{N} \bar{\Omega}_i$; (3) Ω_i is bounded for each $i \neq 0$; (4) $n_b|_{\Omega_i} \in C^1(\bar{\Omega}_i)$ for all $i = 0, \ldots, N$; (5) $n_b(x) = \tilde{n}_0 \in \mathbb{C}$ for $x \in \Omega_0$, with $\mathrm{Im}\{\tilde{n}_0\} \geq 0$; (6) there exists a subset J_0 of the finite set $\{1, 2, \ldots, N\}$ such that $\tilde{\Omega}_0 := \mathrm{int}\left\{x \in \mathbb{R}^2 : n_b(x) = \tilde{n}_0\right\} = \Omega_0 \cup (\cup_{j \in J_0} \Omega_j)$ (in particular, $J_0 = \emptyset$ if and only if $\tilde{\Omega}_0 = \Omega_0$). Finally, we assume that the magnetic permeability is constant on all $\mathbb{R}^2$. Note that (a) the domains Ω_i do not need to be simply connected: e.g., in Figure 1, Ω_3 has Ω_4 as its hole and, in turn, Ω_1 has holes corresponding to Ω_2 and $\Omega_3 \cup \Omega_4$; (b) the boundaries $\partial\Omega_i$ may be either curves where a discontinuity of n_b occurs, or boundaries of virtual domains Ω_i immersed in a homogeneous region, where to host a scatterer that will be introduced later (this trick allows some notational simplifications).

Next, we define the Green's function $G(x; y)$ of the background as the radiating solution of [12]

$$\Delta_x G(x; y) + k^2 n_b(x)\, G(x; y) = -\delta(x - y) \quad \text{for} \quad x \in \mathbb{R}^2, \tag{2.2}$$

where $k = \omega/c$ is the wave number in a vacuum, c being the speed of light in free space. The existence and uniqueness of $G(x; y)$ (at least for $y \in \tilde{\Omega}_0$) can be proved as in [11, 12]: in fact, if we denote the Green's function of the homogeneous medium in $\tilde{\Omega}_0$ by $\Phi(x; y) := \frac{\mathrm{i}}{4} H_0^{(1)}(\tilde{k}_0\, |x - y|)$, where $H_0^{(1)}$ is the Hankel function of first kind of order zero, $\tilde{k}_0 := k\sqrt{\tilde{n}_0}$, and $\mathrm{Im}\{\sqrt{\tilde{n}_0}\} \geq 0$, then we can write

$$G(x; y) = \Phi(x; y) + u_b^s(x; y), \tag{2.3}$$

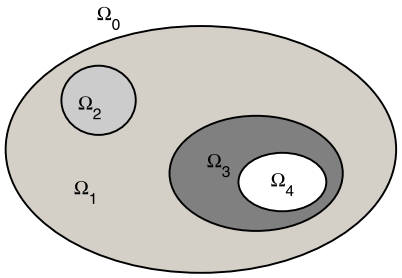

FIG. 1. *Scheme of the reference background for the scattering problem. In this case,* $\tilde{\Omega}_0 = \Omega_0 \cup \Omega_4$.

where $u_b^s(x;y)$ is the perturbation to $\Phi(x;y)$ due to the inhomogeneous medium in $\mathbb{R}^2 \setminus \tilde{\Omega}_0$.

We point out that [12] $G(\cdot;y) \in C^1(\mathbb{R}^2 \setminus \{y\})$; i.e., the discontinuities of n_b across some of the boundaries $\partial\Omega_i$ only affect the smoothness of second (and higher) order derivatives on the boundaries themselves. Actually, (2.2) is to be understood as a set of $N+1$ equations, one for each domain Ω_i, linked by proper transmission conditions at the boundaries $\partial\Omega_i$. These conditions are imposed by physics, which states the continuity of the tangential components of both the total electric field E and the magnetic field H: this is equivalent to the continuity of the vector fields $\nu \times E$ and $\nu \times H$, where "$\times$" denotes the vector product and ν is the unit normal at a point of $\partial\Omega_i$. In our two-dimensional setting, Cartesian axes are chosen so that G is the nonzero component of the total electric field $E = (0,0,G)$, which vibrates perpendicularly to the scattering plane (i.e., the electromagnetic field is assumed to be TM-polarized). Moreover, from the time-harmonic Maxwell equation [11] $\mathrm{curl} E - \mathrm{i}kH = 0$, it follows that $H = \frac{1}{\mathrm{i}k}(\partial_2 G, -\partial_1 G, 0)$, having denoted by ∂_j the partial derivative with respect to the variable x_j for $j = 1,2$. Finally, in the same reference system, the normal ν can be written as $(\nu_1, \nu_2, 0)$; accordingly, $\nu \times E = (\nu_2\, G, -\nu_1\, G, 0)$ and $\nu \times H = (0, 0, -\nu_1\, \partial_1 G - \nu_2\, \partial_2 G)$. Then the continuity of $\nu \times E$ and $\nu \times H$ corresponds to the continuity of G and its normal derivative $\nu \cdot \nabla G = \partial_\nu G$.

In our scattering problem, the scatterer is assumed to take up the spatial region $D = \cup_{i=1}^{M} \Omega_i$, with $1 \le M \le N$; accordingly, the whole propagation medium is described by a refractive index $n(x)$ such that, in general, $n(x) \neq n_b(x)$ for $x \in \Omega_i$, with $i = 1, \ldots, M$. In any case, we still require that $n|_{\Omega_i} \in C^1(\bar{\Omega}_i)$ for all $i = 0, \ldots, N$. Moreover, for a unit point source placed at $x_0 \in \tilde{\Omega}_0 \setminus \overline{(\tilde{\Omega}_0 \cap D)}$, we denote by $u(x;x_0)$ the nonzero component of the total electric field $E = (0,0,u)$, which, as before, vibrates perpendicularly to the scattering plane. Then the differential form of the scattering problem we are interested in is [12]

$$
\begin{cases}
\Delta_x u(x;x_0) + k^2 n(x)\, u(x;x_0) = -\delta(x - x_0) \qquad \text{for } \; x \in \mathbb{R}^2, & \text{(a)} \\
u(x;x_0) = u^i(x;x_0) + u^s(x;x_0), & \text{(b)} \\
\lim\limits_{r\to\infty} \left[\sqrt{r} \left(\dfrac{\partial u^s}{\partial r} - \mathrm{i}\, \tilde{k}_0 u^s \right) \right] = 0, & \text{(c)}
\end{cases}
\tag{2.4}
$$

where $u^i(x;x_0) = G(x;x_0)$ is the incident field, $u^s(x;x_0)$ is the scattered field, and (2.4)(c) is the Sommerfeld radiation condition, which holds uniformly in all directions $\hat{x} = x/|x|$. If $\mathrm{Im}\{\tilde{n}_0\} > 0$, such a condition can be relaxed [12] by only requiring the boundedness of $u^s(\cdot;x_0)$ in $\mathbb{R}^2$.

Note that, from (2.3) and the identification $u^i(x;x_0) = G(x;x_0)$, we can rewrite (2.4)(b) as $u(x;x_0) = \Phi(x;x_0) + [u_b^s(x;x_0) + u^s(x;x_0)]$; then, as before, the existence and uniqueness of a solution $u(\cdot;x_0) \in C^1(\mathbb{R}^2 \setminus \{x_0\})$ to problem (2.4) can be proved as in [12], and (2.4)(a) is again to be regarded as a set of $N+1$ equations, one for each domain Ω_i, with the above transmission conditions at the boundaries $\partial\Omega_i$.

Moreover, since both the incident field $u^i(\cdot;x_0)$ and the total field $u(\cdot;x_0)$ are in $C^1(\mathbb{R}^2 \setminus \{x_0\})$, also the scattered field $u^s(\cdot;x_0)$, expressed by (2.4)(b) as the difference $u(\cdot;x_0) - u^i(\cdot;x_0)$, is in $C^1(\mathbb{R}^2 \setminus \{x_0\})$. Actually, it is not difficult to establish further regularity properties of $u^s(\cdot;x_0)$, i.e., $u^s(\cdot;x_0) \in C^1(\mathbb{R}^2)$ and $\Delta u^s(\cdot;x_0) \in C^1\left(\bar{\Omega}_i\right)$ for all $i = 0, \ldots, N$. To this end, we observe that a simple algebraic manipulation of (2.4)(a) yields

$$\Delta_x u(x;x_0) + k^2 n_b(x) u(x;x_0) = -\delta(x-x_0) + k^2 \tilde{n}_0 \frac{n_b(x) - n(x)}{\tilde{n}_0} u(x;x_0); \tag{2.5}$$

i.e., by setting $m(x) := [n_b(x) - n(x)]/\tilde{n}_0$ and remembering that $\tilde{k}_0 = k\sqrt{\tilde{n}_0}$,

$$\Delta_x u(x;x_0) + k^2 n_b(x) u(x;x_0) = -\delta(x-x_0) + \tilde{k}_0^2 m(x) u(x;x_0). \tag{2.6}$$

By using (2.2) and (2.4)(b), as well as the above identification $u^i(x;x_0) = G(x;x_0)$, (2.6) is easily seen to become

$$\Delta_x u^s(x;x_0) + k^2 n_b(x) u^s(x;x_0) = -\left[-\tilde{k}_0^2 m(x) u(x;x_0)\right]. \tag{2.7}$$

The structure of (2.7), which parallels that of (2.2), allows regarding $u^s(\cdot;x_0)$ as the third component of the electric field $E^s = (0,0,u^s)$ radiated by the equivalent source $-\tilde{k}_0^2 m(x) u(x;x_0)$ in the background medium described by the refractive index n_b. We now note that this equivalent source is compactly supported, since $\operatorname{supp} m$ coincides with the support $\bar{D}$ of the scatterer, which is compact by assumption. On the other hand, by hypothesis, we have that $x_0 \in \tilde{\Omega}_0 \setminus \overline{(\tilde{\Omega}_0 \cap D)}$, i.e., the point x_0 is at a finite distance from the equivalent source. Accordingly, there exists an open neighborhood $U_{x_0} \subset \tilde{\Omega}_0$ of x_0 such that (1) $U_{x_0} \cap \operatorname{supp} m = \emptyset$; (2) both the electric field E^s and the corresponding magnetic field $H^s = \frac{1}{ik}(\partial_2 u^s, -\partial_1 u^s, 0)$ are well-defined and bounded in U_{x_0}. Even more, from the transmission conditions imposed by physics and previously recalled, we can conclude that both $u^s(\cdot;x_0)$ and $\partial_\nu u^s(\cdot;x_0)$ are in $C^0(\bar{U}_{x_0})$. But here the unit normal is arbitrary, since no physical interface, i.e., no discontinuity of the refractive index, occurs inside U_{x_0}, where in fact $n_b(x) = \tilde{n}_0$: then, in particular, $\partial_j u^s(\cdot;x_0) \in C^0(\bar{U}_{x_0})$ for $j = 1,2$. Accordingly, we have that $u^s(\cdot;x_0) \in C^1(\bar{U}_{x_0})$. On the other hand, we know that $u^s(\cdot;x_0) \in C^1(\mathbb{R}^2 \setminus \{x_0\})$; we then conclude that $u^s(\cdot;x_0) \in C^1(\mathbb{R}^2)$.

Finally, from (2.7) we find

$$\Delta_x u^s(x;x_0) = -k^2 n_b(x) u^s(x;x_0) + \tilde{k}_0^2 m(x) u(x;x_0). \tag{2.8}$$

Since, by hypothesis, $n_b, m \in C^1(\bar{\Omega}_i)$ for all $i = 0, \ldots, N$, while $u^s(\cdot;x_0) \in C^1(\mathbb{R}^2)$ and $u(\cdot;x_0) \in C^1(\mathbb{R}^2 \setminus \{x_0\})$, from (2.8) we have $\Delta u^s(\cdot;x_0) \in C^1(\bar{\Omega}_i)$. Indeed, the singularity of $u(x;x_0)$ for $x = x_0$ is cancelled out by $m(x)$, since $x_0 \notin \operatorname{supp} m$ by assumption, while $u^s(\cdot;x_0)$ is bounded at infinity (actually, it is bounded in all $\mathbb{R}^2$ [12]).

Of course, as a particular case (i.e., $n(x) = n_b(x)$ for all $x \in \mathbb{R}^2$) of the above discussion, the same regularity properties also hold for the field $u_b^s(\cdot; y)$ introduced in (2.3), i.e., $u_b^s(\cdot; y) \in C^1(\mathbb{R}^2)$ and $\Delta u_b^s(\cdot; y) \in C^1\left(\bar{\Omega}_i\right)$ for all $i = 0, \ldots, N$.

3. The inhomogeneous Lippmann–Schwinger equation. The goal of the present section is to derive an integral equation for the scattered field $u^s(\cdot; x_0)$ from the differential formulation (2.4) of the scattering problem. Observing the structure of (2.7), the natural candidate for an integral formulation is the "generalized" Lippmann–Schwinger equation

$$u^s(x; x_0) = -\tilde{k}_0^2 \int_{\mathbb{R}^2} G(x; y) m(y) u(y; x_0)\, dy. \tag{3.1}$$

In fact, an exact equivalence between differential and integral formulation is proved in [11] for the three-dimensional acoustic and electromagnetic cases under strong regularity assumptions on the refractive index: the background is assumed to be homogeneous (i.e., $n_b(x) = \tilde{n}_0 \in \mathbb{C}$ for all $x \in \mathbb{R}^3$), and n must be continuously differentiable on the whole space (however, see [17] for a variational approach notably relaxing the latter requirement). In particular, under such assumptions, this proof can provide a rigorous justification of the following procedure: compute $\Delta_x u^s(x; x_0)$ by interchanging the Laplacian operator with the integral in (3.1), then replace

$$\Delta_x \Phi(x; y) = -\tilde{k}_0^2 \Phi(x; y) - \delta(x - y) \tag{3.2}$$

(which is analogous to (2.2) in the homogeneous case $G(x; y) = \Phi(x; y)$) into (3.1) to obtain

$$\Delta_x u^s(x; x_0) + \tilde{k}_0^2 u^s(x; x_0) = -\left[-\tilde{k}_0^2 m(x) u(x; x_0)\right]. \tag{3.3}$$

Equation (3.3) suggests regarding the term in square brackets on the right-hand side as an equivalent, although unknown, source radiating the field $u^s(x; x_0)$ in the homogeneous background, which is consistent with the physical interpretation of (3.1). In any case, by means of (3.2) and (3.3), it is easily verified that u^s, as given by (3.1), solves problem (2.4).

However, as correctly pointed out in [22], even a mere discontinuity of the physical parameters at the interface ∂D between the scatterer and the (homogeneous) background suffices to invalidate, in general, the previous procedure. As a consequence, even with a homogeneous background, the integral formulation becomes more complicated (owing to the occurrence of boundary terms on ∂D) and its equivalence with the differential formulation is more difficult to prove.

To our knowledge, in the case of an inhomogeneous background, results concerning the equivalence between the differential and integral formulation of a scattering problem are not available. In this section, we shall limit ourselves to deriving the integral equation (3.1) (for $x \in \tilde{\Omega}_0$) from the differential problem (2.4); indeed, a thorough discussion of the equivalence between (3.1) and (2.4) would be very technical and beyond the framework of this paper. However, it is likely that an exact equivalence actually holds, since, as recalled above, the scattered field u^s is in $C^1(\mathbb{R}^2)$; then the boundary contributions on each $\partial\Omega_i$ that would appear in (3.1) from Green's second theorem [11] applied in each domain Ω_i cancel out, as detailed in the following Lemma 3.1 and Theorem 3.2 for the case $x \in \tilde{\Omega}_0$.

Finally, it is worth noting that, even in two dimensions, the previous argument fails [22] whenever the magnetic permeability is discontinuous across $\partial\Omega_i$. This is analogous to what happens in the two- or three-dimensional acoustic case [22], where the pressure field is continuous across the discontinuities of the fluid density, but not continuously differentiable.

LEMMA 3.1. *Let Ω_i (with $i = 0, \dots, N$), $\tilde{\Omega}_0$, $n_b(x)$, $G(x;y)$ be as above, let $B_R := \{x \in \mathbb{R}^2 : |x| < R\}$ be such that $B_R \supset \cup_{i=1}^N \bar{\Omega}_i$, and define $\Omega_{N+1} := B_R \backslash \cup_{i=1}^N \bar{\Omega}_i$. Moreover, let $w \in C^1(\bar{B}_R)$ be such that $\Delta w \in C^0(\bar{\Omega}_i)$ for all $i = 1, \dots, N+1$. Then the following generalization of Green's formula holds:*

$$w(x) = \int_{\partial B_R} \left[\frac{\partial w}{\partial \nu}(y) G(y;x) - w(y) \frac{\partial G(y;x)}{\partial \nu(y)} \right] ds(y) - \int_{B_R} \left[\Delta w(y) + k^2 n_b(y) w(y) \right] G(y;x)\, dy \qquad \forall x \in B_R \cap \tilde{\Omega}_0. \tag{3.4}$$

Proof. Consider an arbitrary point $x \in \Omega_R := B_R \cap \tilde{\Omega}_0$. Since Ω_R is open, there exist $\rho > 0$ and a ball $B(x;\rho) := \{y \in \mathbb{R}^2 : |y - x| < \rho\}$ such that $\bar{B}(x;\rho) \subset \Omega_R$. Moreover, $G(\cdot;x)$ solves a particular case of the differential problem (2.4), with the identifications $x_0 = x$, $u(\cdot;x_0) = G(\cdot;x)$, $u^i(\cdot;x_0) = \Phi(\cdot;x)$, and $n = n_b$. Accordingly, remembering (2.3) and the regularity properties stated in the previous section, we have that $G(\cdot;x) \in C^1\left(\bar{B}_R \setminus \{x\}\right)$, $\Delta G(\cdot;x) \in C^1\left(\bar{\Omega}_R \setminus \{x\}\right)$, and $\Delta G(\cdot;x) \in C^1(\bar{\Omega}_i)$ for all $i \in \{1, \dots, N\} \setminus J_0$, where the index set J_0 has been defined in assumption (6) below (2.1). Then, given the regularity properties assumed for w, we can apply the usual Green's second theorem [11, 16] in the domain $\Omega_R \setminus \bar{B}(x;\rho)$, i.e.,

$$\int_{\Omega_R \setminus \bar{B}(x;\rho)} [G(y;x)\Delta w(y) - w(y)\Delta_y G(y;x)]\, dy = \int_{\partial\Omega_R \cup \partial B(x;\rho)} \left[G(y;x) \frac{\partial w(y)}{\partial \nu} - w(y) \frac{\partial G(y;x)}{\partial \nu(y)} \right] ds(y), \tag{3.5}$$

as well as in any other domain Ω_i, with $i \in \{1, \dots, N\} \setminus J_0$, i.e.,

$$\int_{\Omega_i} [G(y;x)\Delta w(y) - w(y)\Delta_y G(y;x)]\, dy = \int_{\partial\Omega_i} \left[G(y;x) \frac{\partial w(y)}{\partial \nu} - w(y) \frac{\partial G(y;x)}{\partial \nu(y)} \right] ds(y). \tag{3.6}$$

In (3.5) and (3.6), it is understood that the unit normal is chosen as outward with respect to each domain. We now sum (3.5) with all the equations (3.6) obtained for $i \in \{1, \dots, N\} \setminus J_0$; note that, except for ∂B_R and $\partial B(x;\rho)$, all the boundary integrals are taken twice, with opposite orientation of the unit normal. Since the integrand functions are continuous on the boundaries, these integrals cancel out. Moreover, by (2.2), we can substitute $\Delta_y G(y;x) = -k^2 n_b(y) G(y;x)$ for $y \neq x$ into (3.5) and (3.6). As a result, we find

$$\int_{B_R \setminus \bar{B}(x;\rho)} \left[\Delta w(y) + k^2 n_b(y) w(y) \right] G(y;x) dy = \int_{\partial B_R \cup \partial B(x;\rho)} \left[G(y;x) \frac{\partial w(y)}{\partial \nu} - w(y) \frac{\partial G(y;x)}{\partial \nu(y)} \right] ds(y). \tag{3.7}$$

We now focus on the integral over $\partial B(x;\rho)$, say $I_{\partial B(x;\rho)}$, on the right-hand side of (3.7). Remembering (2.3), we have

$$I_{\partial B(x;\rho)} = \int_{\partial B(x;\rho)} \left[\Phi(y;x) \frac{\partial w(y)}{\partial \nu} - w(y) \frac{\partial \Phi(y;x)}{\partial \nu(y)} \right] ds(y) + \int_{\partial B(x;\rho)} \left[u_b^s(y;x) \frac{\partial w(y)}{\partial \nu} - w(y) \frac{\partial u_b^s(y;x)}{\partial \nu(y)} \right] ds(y). \tag{3.8}$$

Now, the second integral in (3.8) vanishes as $\rho \to 0$, since the integrand is bounded and the measure of the integration domain tends to zero. As regards the first integral in (3.8), we recall [8] the following asymptotic behaviors:

$$\Phi(y;x) = \frac{1}{2\pi} \ln \frac{1}{|x-y|} + O(1) \qquad \text{as } |x-y| \to 0, \tag{3.9}$$

$$\frac{\partial \Phi(y;x)}{\partial \nu(y)} = \frac{1}{2\pi} \frac{1}{|x-y|} + O(|x-y| \ln |x-y|) \qquad \text{as } |x-y| \to 0. \tag{3.10}$$

By using (3.9) and (3.10), the integral mean value theorem applied to the first integral in (3.8) easily shows that the latter tends to $-w(x)$ as $\rho \to 0$. Then thesis (3.4) is obtained by taking $\rho \to 0$ in (3.7). Indeed, recalling (2.3) and the regularity of $u_b^s(y;x)$, the singularity of $G(y;x)$ for $y \to x$ is only due to $\Phi(y;x)$, i.e., it is weak, and then the integral on B_R converges. □

THEOREM 3.2. *Let Ω_i (with $i = 0, \ldots, N+1$), $\tilde{\Omega}_0$, D, $n_b(x)$, $n(x)$, $m(x)$, $G(x;y)$ be as above, and let $x_0 \in \tilde{\Omega}_0 \setminus (\tilde{\Omega}_0 \cap D)$ be as above. If $u^s(\cdot;x_0) \in C^1(\mathbb{R}^2)$, with $\Delta u^s(\cdot;x_0) \in C^1(\bar{\Omega}_i)$ for all $i = 0, \ldots, N$, is a solution of the differential problem (2.4), then $u^s(\cdot;x_0)$ solves the integral equation (3.1) for $x \in \tilde{\Omega}_0$.*

Proof. Consider an arbitrary point $x \in \tilde{\Omega}_0$. Let $B_R := \{x \in \mathbb{R}^2 : |x| < R\}$ be an open disk with exterior unit normal ν and radius R large enough, so that $B_R \supset \left[\cup_{i=1}^N \bar{\Omega}_i \cup \{x\}\right]$. By hypothesis, $u^s(\cdot;x_0)$ is regular enough in the domain B_R to be represented by means of the generalized Green's formula (3.4) in $\Omega_R := B_R \cap \tilde{\Omega}_0$, i.e.,

$$u^s(x;x_0) = \int_{\partial B_R} \left\{ \frac{\partial u^s(y;x_0)}{\partial \nu(y)} G(y;x) - u^s(y;x_0) \frac{\partial G(y;x)}{\partial \nu(y)} \right\} ds(y) - \int_{B_R} \left\{ \Delta_y u^s(y;x_0) + k^2 n_b(y) u^s(y;x_0) \right\} G(y;x) dy, \qquad x \in \Omega_R. \tag{3.11}$$

First we prove that the integral on ∂B_R in (3.11) is zero. To this end, consider $B_r := \{x \in \mathbb{R}^2 : |x| < r\}$ such that $r > R$, and apply Green's second theorem [11] in the domain $B_r \setminus B_R$. By choosing the unit normal ν as outgoing from both B_R and B_r, and observing that both the fields $u^s(\cdot;x_0)$ and $G(\cdot;x)$ verify the same Helmholtz equation in $B_r \setminus B_R \subset \Omega_0$ (where $n_b(x) = n(x) = \tilde{n}_0$), we find

$$\int_{\partial B_R} \left\{ \frac{\partial u^s(y;x_0)}{\partial \nu(y)} G(y;x) - u^s(y;x_0) \frac{\partial G(y;x)}{\partial \nu(y)} \right\} ds(y) = \int_{\partial B_r} \left\{ \frac{\partial u^s(y;x_0)}{\partial \nu(y)} G(y;x) - u^s(y;x_0) \frac{\partial G(y;x)}{\partial \nu(y)} \right\} ds(y). \tag{3.12}$$

We now recall [11] that any radiating solution v of the Helmholtz equation (with generic wave number $k > 0$) outside a disk in $\mathbb{R}^2$ has asymptotic behavior

$$v(x) = \frac{e^{ikr}}{\sqrt{r}} \left\{ v_\infty(\hat{x}) + O\left(\frac{1}{r}\right) \right\}, \qquad r = |x| \to \infty, \tag{3.13}$$

where v_∞ is the far-field pattern of v. If v^1 and v^2 are two such solutions, from (3.13) we find [11]

$$v^1(x)\frac{\partial v^2(x)}{\partial r} = \mathrm{i}k\frac{e^{2\mathrm{i}kr}}{r}\, v^1_\infty(\hat{x})\, v^2_\infty(\hat{x}) + O\left(\frac{1}{r^2}\right), \qquad r \to \infty, \tag{3.14}$$

uniformly for all directions. By applying (3.14) to the radiating fields $u^s(\cdot; x_0)$ and $G(\cdot; x)$, we easily find that the integrand function on the right-hand side of (3.12) is $O\left(\frac{1}{r^2}\right)$, and then the integral itself vanishes as $r \to \infty$. This is even more true if the wave number $k > 0$ is replaced by $k\sqrt{\tilde{n}_0}$ with $\mathrm{Im}\left\{\sqrt{\tilde{n}_0}\right\} > 0$, since the attenuation of the fields and their derivatives is faster.

As regards the integral on B_R in (3.11), we come back to (2.7) in section 2 and recall that the singularity of $u(x; x_0)$ for $x = x_0$ is cancelled out by $m(x)$, since $x_0 \notin \operatorname{supp} m$. Then, substituting (2.7) into (3.11) and taking the limit as $R \to \infty$, we can write

$$u^s(x; x_0) = -\tilde{k}_0^2 \int_{\mathbb{R}^2} G(y; x) m(y) u(y; x_0)\, dy \qquad \forall x \in \tilde{\Omega}_0, \tag{3.15}$$

which is immediately written in the form (3.1) by using the reciprocity property [12, 19] $G(y; x) = G(x; y)$. □

We call (3.1) the "inhomogeneous Lippmann–Schwinger equation" to emphasize that the reference background is (or may be) inhomogeneous. In the next section, we shall apply an inversion algorithm to this equation in order to compute the point values of m, i.e., of the refractive index inside the region under investigation.

4. A hybrid scheme. In general, iterative methods for the quantitative solution of inverse scattering problems are applied to the homogeneous Lippmann–Schwinger equation. Such methods take as input the scattering data collected by antennas placed outside the investigated area and inside a homogeneous zone and provide as output the reconstruction of the refractive index everywhere in the inhomogeneous region. The main drawback of this computational approach is that, particularly when the scattering experiment is performed with a single and fixed frequency, the number of unknowns is typically much larger than the number of measured data, and therefore the reconstruction accuracy is often rather low. However, there are situations where just a certain part of the inhomogeneous region is unknown and of interest for practical applications, while information is available about the refractive index of the rest of the domain. In this case, the quantitative inverse scattering method can be applied to the inhomogeneous Lippmann–Schwinger equation, provided one is able to compute the Green's function of the inhomogeneous (and known) background and to approximately identify the region taken up by the scatterer under investigation. In the following of the current section, we describe an implementation of this approach essentially based on the contrast source inversion method. Therefore, in order to realize the proposed hybrid approach, the ingredients we need are (1) a method for computing the Green's function of the background; (2) a qualitative method to visualize (an overestimate of) the scatterer support inside the background itself; (3) a quantitative scheme for the inversion of the inhomogeneous Lippmann–Schwinger equation in the region identified at step (2).

4.1. The computation of the Green's function. A handy way to compute the Green's function of an inhomogeneous background is given by the method of moments (MOM) [15, 25]. Since $G(\cdot; x_0)$ solves a particular case of problem (2.4)

with the identifications $u(\cdot;x_0) = G(\cdot;x_0)$, $u^i(\cdot;x_0) = \Phi(\cdot;x_0)$ and $n(x) = n_b(x)$, it also satisfies the homogeneous Lippmann–Schwinger equation [11, 12]

$$G(x;x_0) = \Phi(x;x_0) - \tilde{k}_0^2 \int_{\mathbb{R}^2} \Phi(x;y) m_b(y) G(y;x_0)\, dy \quad \text{for } x \in \mathbb{R}^2, \tag{4.1}$$

with $m_b(x) := [\tilde{n}_0 - n_b(x)]/\tilde{n}_0$ and $x_0 \in \tilde{\Omega}_0$. Since $\operatorname{supp} m_b$ is compact, the integration domain in (4.1) is bounded. Then we can consider a finite (and not necessarily uniform) partition of $\operatorname{supp} m_b$ by L cells $A_1, \ldots, A_L$, chosen so small that m_b and $G(\cdot;x_0)$ can be assumed to be constant inside each cell. Then (4.1) can be approximated as

$$G(x;x_0) \approx \Phi(x;x_0) - \tilde{k}_0^2 \sum_{j=1}^{L} m_b(y_j) G(y_j;x_0) \int_{A_j} \Phi(x;y) dy, \tag{4.2}$$

where $y_j \in \mathbb{R}^2$ identifies the center of the cell A_j. Furthermore, following [25], we approximate each square cell as a circular cell of the same area, so that the integral in (4.2) can be evaluated as

$$\begin{aligned} \int_{A_j} \Phi(x;y) dy &= \frac{\mathrm{i}}{4} \int_{A_j} H_0^{(1)}(\tilde{k}_0 |x-y|) dy \\ &\approx \begin{cases} \dfrac{\mathrm{i}\pi \tilde{k}_0 a_j}{2} J_1(\tilde{k}_0 a_j) H_0^{(1)}(\tilde{k}_0 |x-y_j|) & \text{for } x \notin A_j, \\ \dfrac{\mathrm{i}}{2}\left[\pi \tilde{k}_0 a_j H_1^{(1)}(\tilde{k}_0 a_j) + 2\mathrm{i}\right] & \text{for } x \in A_j, \end{cases} \end{aligned} \tag{4.3}$$

where $a_j := \sqrt{\Delta_j/\pi}$, Δ_j is the area of the cell A_j, J_1 is the Bessel function of first order, and $H_1^{(1)}$ is the Hankel function of first kind of order one. We point out that the method can be notably sped up by utilizing the fast Fourier transform algorithm as described, for example, in [4, 29]. We shall adopt this version of the MOM method for our numerical simulations.

4.2. The linear sampling method. The linear sampling method (LSM) is the earliest and most used qualitative method in inverse scattering. In the case of an object embedded in a homogeneous background, it provides a reconstruction of its support by knowing only the field measured around it. When the background is inhomogeneous and its Green's function is known, the LSM can be extended to the case of an inhomogeneity immersed in a medium with piecewise constant refractive index. The basic idea is to write and to approximately solve the modified far-field equation [9, 12]

$$\int_{\Gamma} [u^s(x;x_0) - u_b^s(x;x_0)] g_z(x_0)\, dx_0 = G(x;z) \quad \text{for } x \in \Gamma, \tag{4.4}$$

where $\Gamma := \{x \in \mathbb{R}^2 : |x| = R_\Gamma\} \subset \Omega_0$ is the circle of radius R_Γ where emitting and receiving antennas are placed, and $z \in \mathbb{R}^2$ is a sampling point inside the investigation domain enclosed by Γ. In (4.4), the Green's function $G(x;z)$ and the field $u_b^s(x;x_0)$ can be computed by exploiting the knowledge of the background and applying the MOM, while $u^s(x;x_0)$ represents the measurements, i.e., the data of the inverse scattering problem.

In fact, it can be proved [9, 12] that there exists an approximate solution of (4.4) whose $L^2(\Gamma)$-norm is bounded inside the scatterer, grows up as z approaches

its boundary from inside, and remains very large outside, thus behaving as an indicator function for the support $\bar{D}$ of the scatterer itself. This result inspires a simple algorithm that approximately solves the modified far-field equation by means of a regularization procedure. More precisely, the LSM requires the choice of a numerical grid covering the region where the scatterer is placed; then, for each point z of the grid, a discretized version of the modified far-field equation is solved by using the Tikhonov regularization method [26], and the Euclidean norm of the regularized solution is plotted for each z. As a result, the boundary of the scatterer is highlighted by the points of the grid corresponding to the largest increase of the Euclidean norm. We recall that the computational time of this algorithm can be notably reduced by applying a no-sampling formulation [2], called the no-sampling linear sampling method (NSLSM), which is the one adopted in the present paper.

Finally, we remark that, for the purposes of our implementation, a univocal identification of the shape of the scatterer is performed by postprocessing the NSLSM through an active contour technique [1, 10]; for reasons that will be clear in the next subsection, we choose the parameters of this edge detection algorithm in such a way that a slight overestimate of the scatterer is favored.

4.3. The contrast source inversion method. In our hybrid scheme, the contrast source inversion (CSI) method [14, 27, 28] is the technique we use for the quantitative inversion of the inhomogeneous Lippmann–Schwinger equation. More precisely, the CSI method computes the point values of the refractive index $n(x)$ inside an investigation domain T containing the scatterer support $\bar{D} = \operatorname{supp} m$. The idea at the basis of the CSI method is to split an inverse scattering problem described by an integral equation such as (3.1) into two different problems, one defined inside T and the other one on the curve Γ where antennas are placed. More formally, remembering (2.4)(b), equation (3.1) is equivalently recast in the form

$$u(x;x_0) = u^i(x;x_0) - \tilde{k}_0^2 \int_T G(x;y) m(y) u(y;x_0)\, dy \tag{4.5}$$

and then replaced by the system

$$\begin{cases} w(x;x_0) = m(x)u^i(x;x_0) - m(x)\left[\mathcal{G}^T w(\cdot;x_0)\right](x) & \text{for } x \in T, \quad \text{(a)} \\ u^s(x;x_0) = -\left[\mathcal{G}^\Gamma w(\cdot;x_0)\right](x) & \text{for } x \in \Gamma, \quad \text{(b)} \end{cases} \tag{4.6}$$

where $w(x;x_0) := m(x)u(x;x_0)$, the operator $\mathcal{G}^T : L^2(T) \to L^2(T)$ is defined as

$$\left[\mathcal{G}^T f\right](x) := \tilde{k}_0^2 \int_T G(x;z) f(z)\, dz \qquad \forall x \in T, \tag{4.7}$$

and $\mathcal{G}^\Gamma : L^2(T) \to L^2(\Gamma)$ is defined as

$$\left[\mathcal{G}^\Gamma f\right](x) := \tilde{k}_0^2 \int_T G(x;z) f(z)\, dz \qquad \forall x \in \Gamma. \tag{4.8}$$

Note that (4.6)(a) is obtained from (4.5) by multiplying both members for $m(x)$, while (4.6)(b) is the restriction of (3.1) for $x \in \Gamma$; in particular, $u^s(x;x_0)$ for $x \in \Gamma$ represents the data of the inverse scattering problem.

The CSI method consists of minimizing the functional

$$F(w,m) = \frac{\|u^s - \mathcal{G}^\Gamma w\|_\Gamma^2}{\|u^s\|_\Gamma^2} + \frac{\|mu^i - w - m\,\mathcal{G}^T w\|_T^2}{\|mu^i\|_T^2}, \tag{4.9}$$

where we dropped the dependence on x, x_0, and $\|\cdot\|_\Gamma$, $\|\cdot\|_T$ denote the L^2-norms on the spaces $L^2(\Gamma)$, $L^2(T)$, respectively. The minimization of F is performed by applying gradient algorithms [24] and the updates are alternately computed for m and w [27, 28]. The information on the background is again coded into the Green's function, i.e., into the operators $\mathcal{G}^T$ and $\mathcal{G}^\Gamma$.

In the standard case of a homogeneous medium, the implementation of the approach described above is well established and does not require further discussion. Instead, in the inhomogeneous case two issues need to be addressed. First, we observe that (4.6)(a) is written for $x \in T$; on the other hand, the integral equation (3.1), whence (4.6)(a) should derive, has been proved in Theorem 3.2 only for $x \in \tilde{\Omega}_0$ and, in general, T is not contained in $\tilde{\Omega}_0$. To overcome this drawback, we observe that the purpose of the CSI algorithm is to compute the values of $n(x)$ for $x \in T$, and these values do not depend on the reference background inside T. Then we can think that the original background in T is replaced by an artificial one, which hosts the same homogeneous medium occupying $\tilde{\Omega}_0$. In other words, this amounts to replacing the refractive index n_b with $\tilde{n}_b$, such that $\tilde{n}_b(x) = \tilde{n}_0$ for all $x \in T$ and $\tilde{n}_b(x) = n_b(x)$ for all $x \notin T$. Of course, the background Green's function $G(x; z)$ in (4.7) and (4.8) must be replaced accordingly, i.e., by $\tilde{G}(x; z)$. We point out that a good choice of the investigation domain T is the region highlighted by the NSLSM, as explained in subsection 4.2. Indeed, such a region is an overestimate of D; i.e., it contains D, but is also close to being as small as possible, thus minimizing the number of points where $n(x)$ is to be computed, i.e., the number of unknowns of the problem. As a result, also the number of measurements necessary for a successful implementation of the method is optimized.

This same trick, i.e., changing the background as just explained, is also useful to address the second issue, which is concerned with the computation of the Green's function $G(x; z)$. Indeed, (4.7) shows that both x and z vary in T. Then, in particular, also the singular case $x = z$ is of interest. Now, $G(x; z)$ satisfies (4.1) (with the identification $z = x_0$), which implies that if $z \in \operatorname{supp} m_b$ and $x = z$, the integrand function on the right-hand side of (4.1) is affected by a double singularity for $y = z$: one due to $\Phi(z; y)$, the other one due to $G(y; z)$. This prevents us from applying the usual approximation scheme outlined in eqs. (4.2) and (4.3). Accordingly, an ad hoc quadrature rule should be created to numerically compute the integral. Such a problem is avoided by the previous choice of the new background, i.e., of $\tilde{n}_b$. Indeed, the region T is now erased by the actual integration domain in (4.1), since $\tilde{m}_b(x) := [\tilde{n}_0 - \tilde{n}_b(x)]/\tilde{n}_0$ vanishes inside T, while $z \in T$.

We are now ready to present in the next section some numerical results obtained by implementing the theoretical framework developed so far.

5. Numerical examples. The aim of this section is twofold. First, we numerically validate the CSI algorithm in the inhomogeneous case. More precisely, we compare the performance of the CSI algorithm based on the inhomogeneous Lippmann–Schwinger equation with that of the traditional CSI algorithm (the two algorithms will be called "inhomogeneous CSI" and "homogeneous CSI," respectively). To this end, we perform a preliminary set of simulations by using simple numerical phantoms and without adding noise to our measurements. Second, we test the effectiveness of the whole hybrid scheme presented above, as well as its worthiness in real-life applications, by implementing it with a realistic phantom of a female breast slice: the goal is to highlight the presence of a tumoral mass inside the inhomogeneous background formed by the healthy tissues.

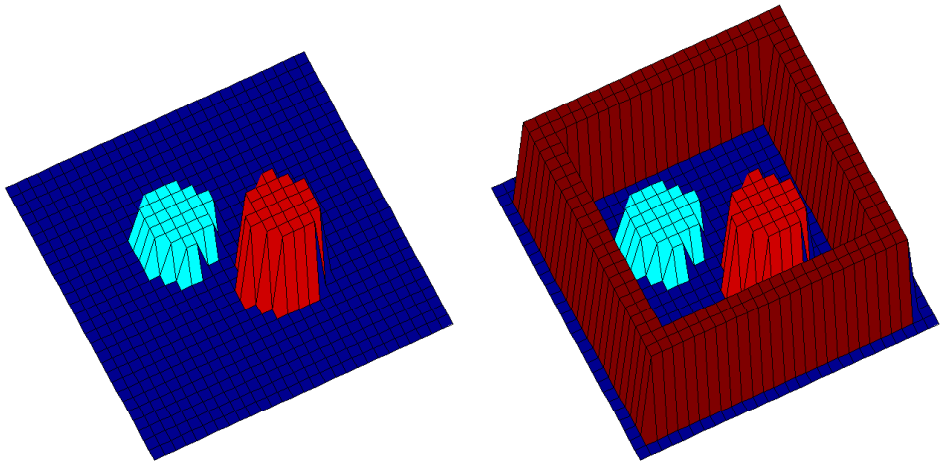

(a) (b)

FIG. 2. *Visualization of the relative dielectric permittivity ε_r of the numerical phantoms utilized for the first set of scattering experiments. The phantoms are piecewise homogeneous and purely dielectric, i.e., nonabsorbing.*

5.1. Homogeneous and inhomogeneous CSI: A comparison. The first set of numerical simulations is concerned with the reconstruction of the two (nonabsorbing) phantoms visualized in panels (a) and (b) of Figure 2. In particular, we are going to show an example where homogeneous CSI fails to provide a satisfactory result, while inhomogeneous CSI succeeds. This is obtained by coding some additional information into the background, which then becomes inhomogeneous.

Indeed, consider first the phantom in Figure 2(a). The pixel values of the relative dielectric permittivity ε_r and the geometry of the objects are plotted in Figure 3(a). The scattering experiment is simulated by choosing a wavelength λ equal to the length unit adopted for all panels in Figure 3, and by using 30 unit point sources uniformly placed on a circle centered at the origin and with radius $3\,\lambda$. The scattered field is computed by means of a MOM code, as outlined in subsection 4.1, at 30 points obtained from the previous ones after a rotation of $\pi/30$. Then we apply homogeneous CSI (implemented in the error-reducing version of [28] and initialized by backpropagation). As a result, we obtain the satisfactory reconstruction shown in Figure 3(b).

However, if we consider the more complex scenario of Figure 2(b), with pixel values of ε_r plotted in Figure 3(c), the same homogeneous CSI provides the unsatisfactory reconstruction shown in Figure 3(d); it is evident that the algorithm converges to the wrong local minimum. A feasible way to overcome this drawback is to consider the square barrier surrounding the two disks as a part of the background; this situation is represented in Figure 3(e). Then we implement the inhomogeneous CSI; in particular, the reconstruction is now performed only inside the barrier, i.e., inside the green square highlighted in Figure 3(f). As a result, the effectiveness of the algorithm in reconstructing the two disks is restored, as shown by Figure 3(f) itself.

5.2. The hybrid approach validated against a realistic numerical breast phantom. In the following numerical examples we test the effectiveness of the hybrid scheme described in section 4 when applied to scattering situations that might occur in practice. To this end, we consider a realistic numerical phantom of a female

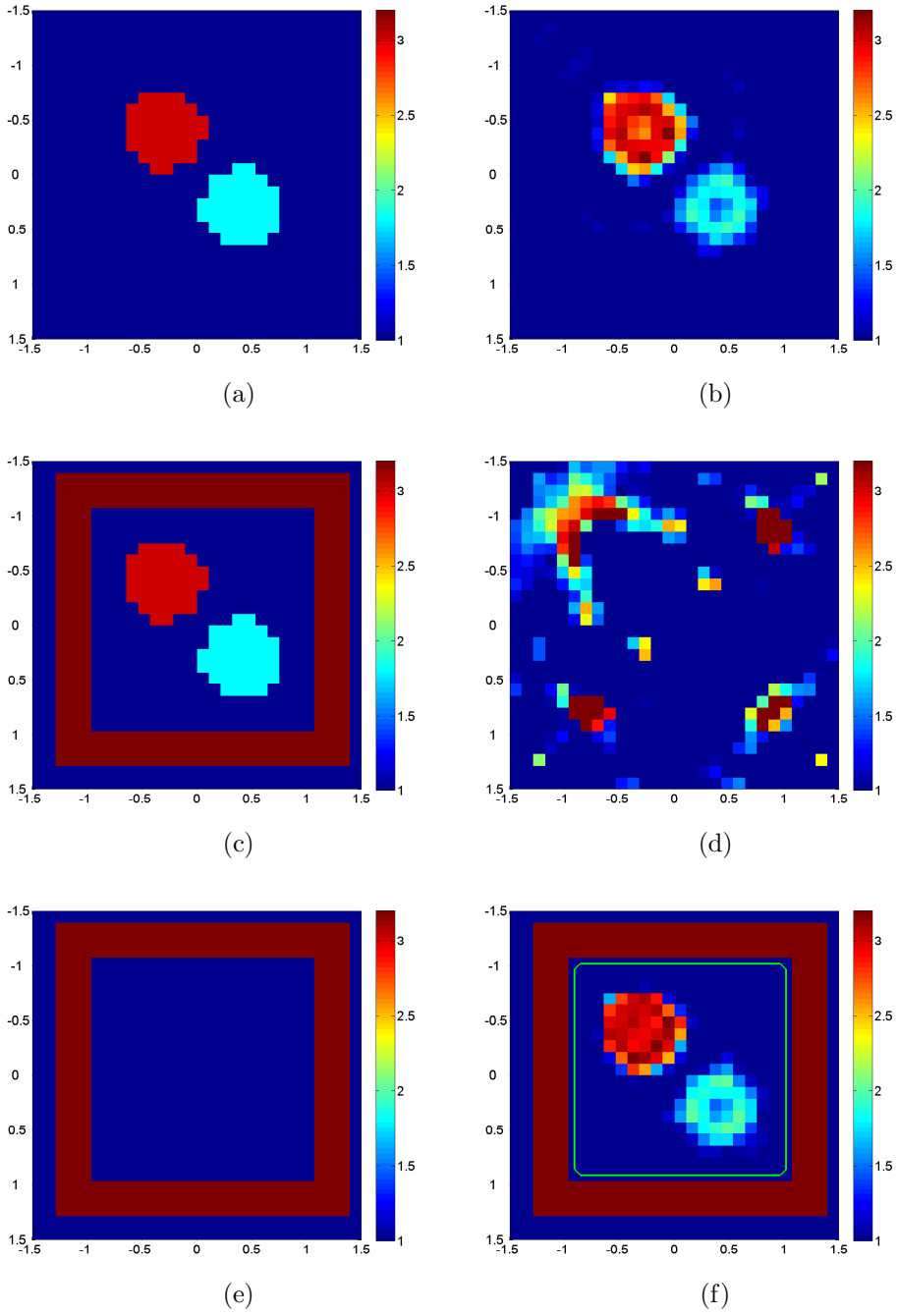

FIG. 3. *Panels* (a) *and* (c)*: pixel values of the relative dielectric permittivity* ε_r *of the phantoms shown in Figure* (a) *and Figure* (b)*, respectively. Panels* (b) *and* (d)*: corresponding reconstructions provided by homogeneous CSI. Panel* (f)*: reconstruction of the phantom in* (c) *provided by inhomogeneous CSI, when the background is assumed to be as shown in panel* (e)*.*

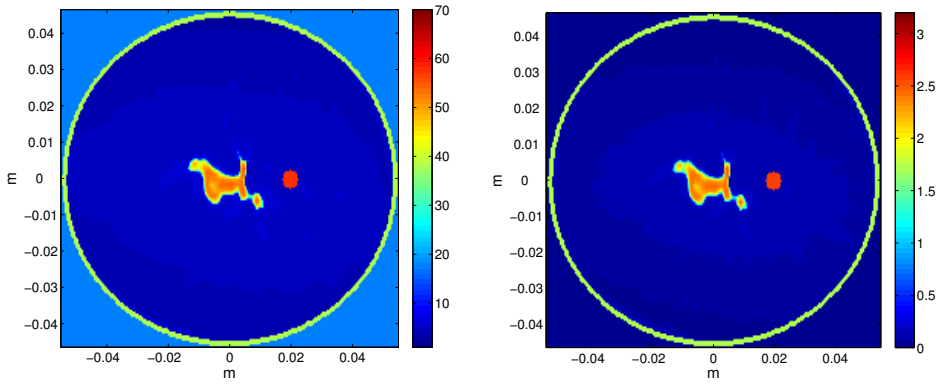

(a) (b)

FIG. 4. *Numerical phantom of the breast slice utilized in our scattering simulations, performed at a frequency of* $f = 3\,GHz$. *Panel* (a)*: pixel values of the relative dielectric permittivity* ε_r. *Panel* (b)*: pixel values of the conductivity* σ. *In both panels, the tumoral mass is the small disk centered at* $(0.02, 0)\,m$ *and with a diameter of* $0.5\,cm$.

breast slice, whose pixel values of relative permittivity ε_r and conductivity σ are obtained from the segmentation of MRI (magnetic resonance imaging) images [20] (such phantoms are downloadable from the website uwcem.ece.wisc.edu/home.htm). Then a circular tumor with a diameter of 0.5 cm is artificially inserted into the phantom; we refer the reader to, e.g., [21] for the values of the electric parameters of tumoral tissues at various frequencies. Our numerical experiments are performed at a frequency of $f = 3$ GHz; accordingly, in panels (a) and (b) of Figure 4 we plot the pixel values of the relative permittivity ε_r and conductivity σ of the breast tissues at such a frequency. As shown in this figure, we also assume that the breast slice is immersed in an infinite and homogeneous coupling medium [23]; this trick reduces reflection phenomena, thus favoring the penetration of the wave into the breast itself. Finally, we choose 30 unit point sources uniformly placed on a circle surrounding the breast, concentric with it and having a radius of 6 cm. By using a MOM code, the scattered field is computed at 30 points obtained from the previous ones after an angular shift of $\pi/30$; then these field values are perturbed by 3% Gaussian noise.

A whole and precise reconstruction of such a heterogeneous scatterer as a breast slice is extremely difficult to be achieved: the main issue is the strong variability of the refractive index from point to point, as well as its large range of values. Then, in order to properly describe the heterogeneity of the tissues, the investigation domain should be discretized by using a large number of pixels, which corresponds to a large number of unknowns in the CSI algorithm. In practical applications, this number can be too large with respect to the amount of data, thus impairing the reliability of the reconstruction. Therefore, an inhomogeneous-background approach to the problem can be helpful. Indeed, when a priori known, a part of the scatterer can be included in the background, so that the reconstruction can be performed on fewer pixels (i.e., in a smaller investigation domain), which reduces the number of unknowns and increases the quality of the reconstruction itself.

In the first numerical example, whose results are collected and visualized in Figure 5, we assume that the known background is formed by the fat internal tissue, the skin layer, and the coupling medium. In general, we may think that such prelimi-

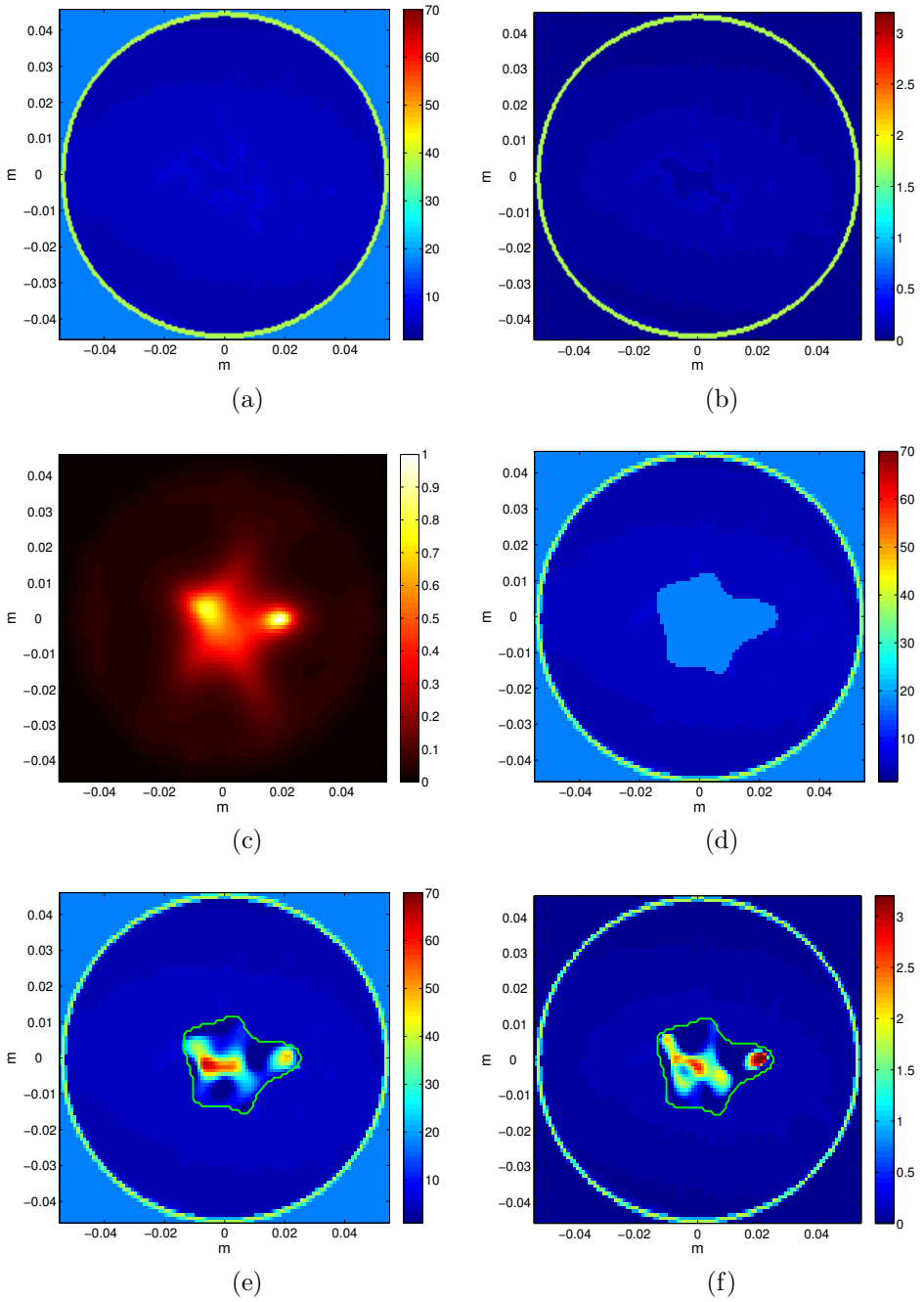

FIG. 5. *Reconstruction of the glandular and tumoral tissues by means of the hybrid approach. Panels* (a) *and* (b)*: pixel values of the relative permittivity* ε_r (a) *and conductivity* σ (b) *of the background utilized for the implementation of the NSLSM. Panel* (c)*: visualization provided by the NSLSM. Panel* (d)*: pixel values of the relative permittivity of the artificial background utilized for the implementation of inhomogeneous CSI; the homogeneous inner domain* T *having the same properties of the outer coupling medium is obtained by applying an active contour technique to the visualization map shown in panel* (c)*. Panels* (e) *and* (f)*: relative permittivity* (e) *and conductivity* (f) *as reconstructed by inhomogeneous CSI; the region of reconstruction, delimited by a closed green line, coincides with the investigation domain* T *identified in panel* (d)*.*

nary information on the tissues is obtained from the segmentation of the most recent MRI image of the patient's breast, while the properties of the coupling medium are known a priori. The pixel values of the relative permittivity ε_r and conductivity σ of these media are shown in panels (a) and (b) of Figure 5. Since our goal here is to reconstruct both the glandular and tumoral tissues inside the breast fat, such background panels have been respectively obtained from panels (a) and (b) of Figure 4 by removing the artificial circular tumor (i.e., by restoring the original healthy tissue) and by artificially replacing the central glandular mass with an "average fat" (i.e., by replacing the pixel values of ε_r and σ in the glandular tissue with constant values computed by averaging over the pixel values of ε_r and σ in the fat tissue). Then this background is utilized to implement the NSLSM, the qualitative technique outlined in subsection 4.2. In Figure 5(c) we show the visualization of the unknown region as provided by the NSLSM; more precisely, we plot the values of the indicator function, chosen as the reciprocal of the squared norm of the regularized solution to the modified far-field equation (4.4). Next, we apply an active contour technique [1, 10] to this visualization map: as a result, we extract the support of the unknown region T, which is the homogeneous inner domain shown in panel (d) of Figure 5. More precisely, in this panel we plot the pixel values of ε_r characterizing the artificial background we need to consider for applying the inhomogeneous CSI in the investigation domain T (the plot of σ would be analogous and is not shown here). Indeed, we recall that, in order to avoid the theoretical and computational problems described in subsection 4.3, the domain T should be considered as filled with the outmost medium (i.e., in our case, with the coupling medium). The reconstructions provided by inhomogeneous CSI inside T for the relative permittivity and for the conductivity are presented in panels (e) and (f) of Figure 5, respectively. The results are in rather good agreement with the true phantoms of Figure 4.

In the second numerical example, we utilize inhomogeneous CSI to investigate the nature of a small inhomogeneity detected by the NSLSM. In this case, while maintaining the coupling medium as before, the whole healthy breast slice, just as provided by the segmentation of the MRI image, is assumed as background, and the reconstruction is performed only on the pixels where the presence of the (prospective) tumor is highlighted (for a detailed analysis of the performance of the NSLSM in this framework, see [5]). As before, panels (a), (b), and (c) of Figure 6 are concerned with the NSLSM: (a) and (b) are the plots of the relative permittivity and conductivity of the background, while (c) shows the NSLSM output, whence the investigation domain T (containing the inhomogeneity to be analyzed) is extracted by using active contours. In panel (d) of Figure 6 we plot the relative permittivity of the artificial background utilized for inhomogeneous CSI: the coupling medium is now inserted into the area T detected by the NSLSM. Finally, panels (e) and (f) show the reconstructions of the relative permittivity and conductivity provided by the inhomogeneous CSI inside T. Again, a comparison with the true phantoms of Figure 4 highlights that the quality of these reconstructions is rather good.

6. Conclusions and further developments. In this paper we have proposed a hybrid method to numerically solve a large class of two-dimensional inverse scattering problems. According to this hybrid approach, a qualitative method, i.e., the NSLSM, is first applied to approximately identify the region of primary interest inside an inhomogeneous background; then a quantitative algorithm, i.e., the inhomogeneous CSI, is implemented only in this region to compute the point values of the electric parameters (permittivity and conductivity) of the unknown scatterer. Both steps

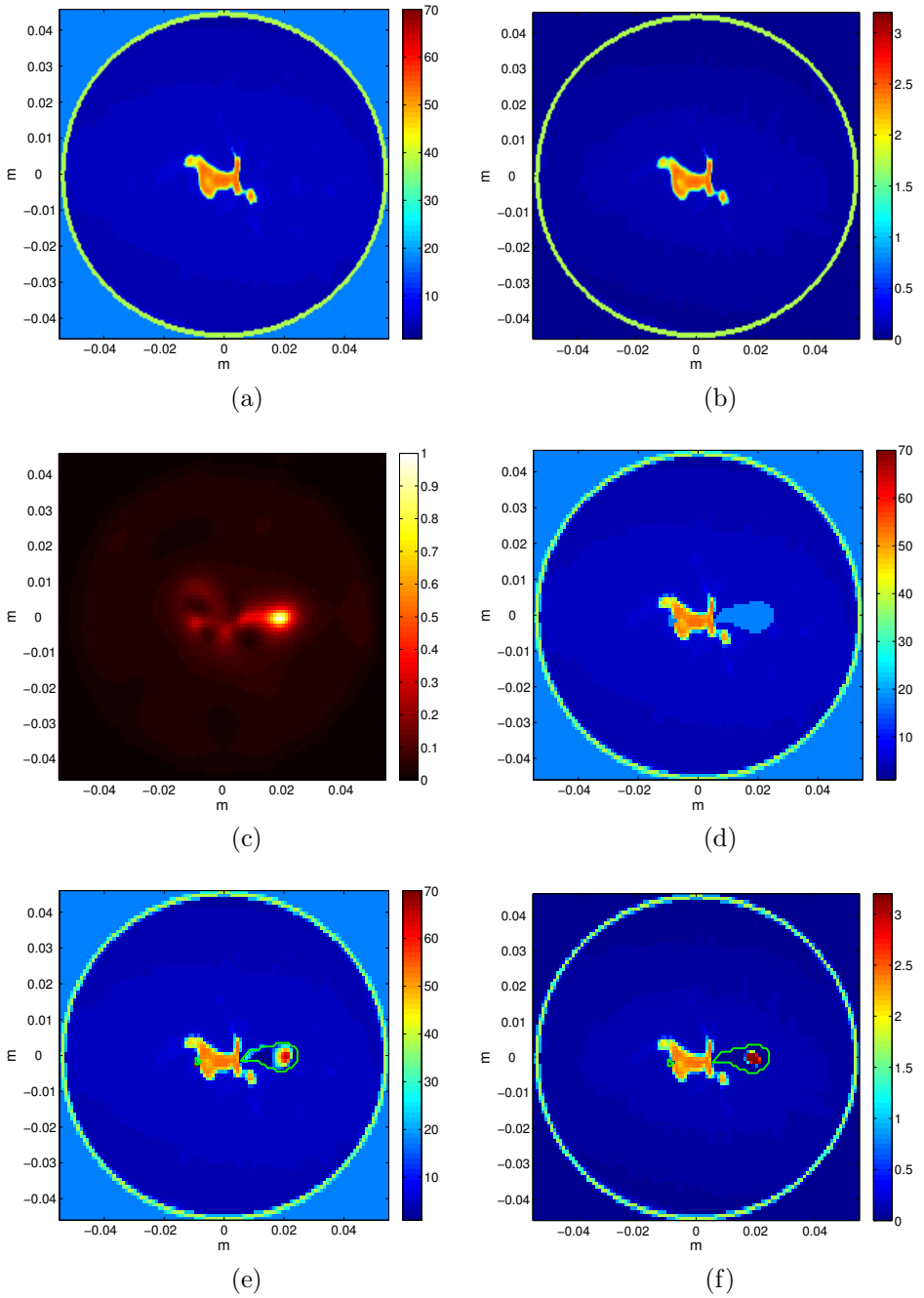

FIG. 6. *Reconstruction of just the tumoral tissue by means of the hybrid approach. Panels* (a) *and* (b)*: pixel values of the relative permittivity* ε_r (a) *and conductivity* σ (b) *of the background utilized for the implementation of the NSLSM. Panel* (c)*: visualization provided by the NSLSM. Panel* (d)*: pixel values of the relative permittivity of the artificial background utilized for the implementation of inhomogeneous CSI; the (nonconnected) homogeneous inner domain* T *having the same properties of the outer coupling medium is obtained by applying an active contour technique to the visualization map shown in panel* (c)*. Panels* (e) *and* (f)*: relative permittivity* (e) *and conductivity* (f) *as reconstructed by inhomogeneous CSI; the region of reconstruction, delimited by two closed green lines (a larger one on the right and a very small one on the left of the glandular tissue), coincides with the investigation domain* T *identified in panel* (d).

are made possible by the knowledge of the inhomogeneous background: inserting such information into the whole procedure improves the quality of the reconstruction and optimizes the amount of data necessary for a satisfactory result, as shown by the numerical simulations in section 5. The first (qualitative) step consists of a no-sampling implementation of the LSM for an inhomogeneous background, which can be performed according to the guidelines recalled in subsection 4.2 and detailed in the papers cited there. Instead, the second (quantitative) step requires a preliminary theoretical investigation, in order to extend the usual Lippmann–Schwinger equation to the case of an inhomogeneous background. Such a generalization has been obtained in section 3 as a consequence of the differential formulation of the scattering problem. Under appropriate assumptions on the refractive index and on the magnetic permeability, the new integral equation maintains its simplest form, i.e., involves no boundary terms across the discontinuities of the electric parameters. Accordingly, the homogeneous and inhomogeneous Lippmann–Schwinger equations have the same structure; this has suggested the idea of generalizing the CSI algorithm, originally based on the former equation, to the case of an inhomogeneous background, handled by the latter.

As regards possible further developments, a first task is trying to prove the exact equivalence between differential and integral formulation of the scattering problem (possibly by adopting a variational approach, i.e., by interpreting system (2.4) in a weak sense and looking for its solution in an appropriate Sobolev space; cf. [17]). As pointed out in section 3, such equivalence is likely to hold. As a generalization, the case of nonconstant magnetic permeability $\mu(x)$ would also deserve an analogous investigation: the corresponding integral formulation would be more complex, owing to the presence of boundary terms across the discontinuities of $\mu(x)$. Of course, the same problems can also be formulated in a three-dimensional framework. An ideal goal might be to parallel and generalize to the case of an inhomogeneous background the results obtained in [22] for a homogeneous one. This would allow extending our hybrid approach to very general three-dimensional inverse scattering problems, where the issues of a good balance between the amount of data and the number of unknowns, as well as the related problem of computational costs, are even more important than in two-dimensional setups.

REFERENCES

[1] R. Aramini, M. Brignone, J. Coyle, and M. Piana, *Postprocessing of the linear sampling method by means of deformable models*, SIAM J. Sci. Comput., 30 (2008), pp. 2613–2634.

[2] R. Aramini, M. Brignone, and M. Piana, *The linear sampling method without sampling*, Inverse Problems, 22 (2006), pp. 2237–2254.

[3] A. B. Bakushinsky and M. Y. Kokurin, *Iterative Methods for Approximate Solution of Inverse Problems*, Springer, Dordrecht, 2004.

[4] G. Bozza, *Numerical Methods for Inverse and Ill-Posed Problems in Electromagnetics*, Ph.D. Thesis, Electronic and Computer Engineering and Telecommunications, Università degli Studi di Genova, 2009.

[5] G. Bozza, M. Brignone, and M. Pastorino, *Application of the no-sampling linear sampling method to breast cancer detection*, IEEE Trans. Biomed. Eng., 57 (2010), pp. 2525–2534.

[6] M. Brignone, G. Bozza, A. Randazzo, M. Piana, and M. Pastorino, *A hybrid approach to 3D microwave imaging by using linear sampling and ACO*, IEEE Trans. Antennas and Propagation, 56 (2008), pp. 3224–3232.

[7] M. Brignone, J. Coyle, and M. Piana, *The use of the linear sampling method for obtaining super-resolution effects in Born approximation*, J. Comput. Appl. Math., 203 (2007), pp. 145–158.

[8] F. Cakoni and D. Colton, *Qualitative Methods in Inverse Scattering Theory*, Springer, Berlin, 2006.

[9] F. Cakoni, M. Fares, and H. Haddar, *Analysis of two linear sampling methods applied to electromagnetic imaging of buried objects*, Inverse Problems, 22 (2006), pp. 845–867.
[10] T. F. Chan and L. A. Vese, *Active contour without edges*, IEEE Trans. Image Process., 10 (2001), pp. 266–277.
[11] D. Colton and R. Kress, *Inverse Acoustic and Electromagnetic Scattering Theory*, 2nd ed., Springer, Berlin, 1998.
[12] D. Colton and P. Monk, *A linear sampling method for the detection of leukemia using microwaves*, SIAM J. Appl. Math., 58 (1998), pp. 926–941.
[13] D. Colton, M. Piana, and R. Potthast, *A simple method using Morozov's discrepancy principle for solving inverse scattering problems*, Inverse Problems, 13 (1997), pp. 1477–1493.
[14] C. Gilmore, A. Abubakar, W. Hu, T. M. Habashy, and P. M. van den Berg, *Microwave biomedical data inversion using the finite-difference contrast source inversion method*, IEEE Trans. Antennas and Propagation, 57 (2009), pp. 1528–1538.
[15] R. F. Harrington, *Field Computation by Moments Methods*, IEEE Press, Piscataway, NJ, 1993.
[16] O. D. Kellogg, *Foundations of Potential Theory*, Springer, Berlin, 1967.
[17] A. Kirsch, *An Introduction to the Mathematical Theory of Inverse Problems*, 2nd ed., Springer, New York, 2011.
[18] R. Kress and P. Serranho, *A hybrid method for sound-hard obstacle reconstruction*, J. Comput. Appl. Math., 204 (2007), pp. 418–427.
[19] L. D. Landau and E. M. Lifshitz, *Electrodynamics of Continuous Media*, 2nd ed., Course Theoret. Phys. 8, Pergamon Press, Oxford, 1984.
[20] M. Lazebnik, L. McCartney, D. Popovic, C. B. Watkins, M. J. Lindstrom, J. Harter, S. Sewall, A. Magliocco, J. H. Booske, M. Okoniewski, and S. C. Hagness, *A large-scale study of the ultrawideband microwave dielectric properties of normal breast tissue obtained from reduction surgeries*, Phys. Med. Biol., 52 (2007), pp. 2637–2656.
[21] M. Lazebnik, M. Okoniewski, J. H. Booske, and S. C. Hagness, *Highly accurate Debye models for normal and malignant breast tissue dielectric properties at microwave frequencies*, IEEE Microw. Wireless Compon. Lett., 17 (2007), pp. 822–824.
[22] P. A. Martin, *Acoustic scattering by inhomogeneous obstacles*, SIAM J. Appl. Math., 64 (2003), pp. 297–308.
[23] P. M. Meaney, S. A. Pendergrass, M. W. Fanning, D. Li, and K. D. Paulsen, *Importance of using a reduced contrast coupling medium in 2D microwave breast imaging*, J. Electromagn. Waves Appl., 17 (2003), pp. 333–355.
[24] E. Polak, *Optimization*, Appl. Math. Sci. 124, Springer, New York, 1997.
[25] J. H. Richmond, *Scattering by a dielectric cylinder of arbitrary cross section shape*, IEEE Trans. Antennas and Propagation, 13 (1965), pp. 334–341.
[26] A. N. Tikhonov, A. V. Goncharski, V. V. Stepanov, and A. G. Yagola, *Numerical Methods for the Solution of Ill-Posed Problems*, Kluwer Academic, Dordrecht, 1995.
[27] P. M. van den Berg and R. E. Kleinmann, *A contrast source inversion method*, Inverse Problems, 13 (1997), pp. 1607–1620.
[28] P. M. van den Berg, A. L. van Broekhoven, and A. Abubakar, *Extended contrast source inversion*, Inverse Problems, 15 (1999), pp. 1325–1344.
[29] Q. Z. Zhong, H. L. Qing, C. Xiao, E. Ward, G. Ybarra, and W. T. Joines, *Microwave breast imaging: 3-D forward scattering simulation*, IEEE Trans. Biomed. Eng., 50 (2003), pp. 1180–1189.